Theory and experiment of differential acoustic resonance spectroscopy

AGU PUBLICATIONS

JGR

Journal of Geophysical Research: Solid Earth

RESEARCH ARTICLE
10.1002/2015JB012297

Special Section:
Stress, Strain and Mass Changes at Volcanoes

Theory and experiment of Differential Acoustic Resonance Spectroscopy

Bouko B. S. A. Vogelaar[1,2], David M. J. Smeulders[2], and Jerry M. Harris[1]

[1]Department of Geophysics, Stanford University, Stanford, California, USA, [2]Faculty of Mechanical Engineering, Eindhoven University of Technology, Eindhoven, Netherlands

Key Points:
- A variety of rock samples are measured in DARS experiments
- A quasi-static poroelastic model is derived
- Predictions agree with experiments on medium to high permeable rocks

Correspondence to:
B. B. S. A. Vogelaar,
b.b.s.a.vogelaar@tue.nl

Citation:
Vogelaar, B. B. S. A., D. M. J. Smeulders, and J. M. Harris (2015), Theory and experiment of Differential Acoustic Resonance Spectroscopy, *J. Geophys. Res. Solid Earth*, *120*, 7425–7439, doi:10.1002/2015JB012297.

Received 7 JUL 2015
Accepted 11 OCT 2015
Accepted article online 16 OCT 2015
Published online 13 NOV 2015

Abstract Recent advances in Differential Acoustic Resonance Spectroscopy (DARS) techniques have given rise to applications in the field of poromechanics. We report on the experimental demonstration of bulk modulus measurements on poroelastic samples at sonic frequencies (1 kHz) with DARS. Normal mode perturbation is due to scattering of a foreign object (i.e., a rock sample) within an otherwise fluid-filled resonator. The perturbation theory on an elastic object determines its bulk modulus (inverse compressibility). The experimental bulk modulus of medium- to high-permeability (>10 mD) poroelastic samples is in agreement with predictions from quasi-static loading of a porous sphere using the Biot theory. This result demonstrates that pore fluid flow governs the dominant relaxation process of the rock during compression. For low-permeability samples (<10 mD), pressure equilibration via slow wave diffusion is limited, and only qualitative agreement is found between the upper bound (Gassmann undrained modulus) and the lower bound (volume-weighted compressibilities of the two constituents). DARS experiments, in conjunction with the poroelastic theory presented here, allow one to infer such rock physical properties as the effective bulk modulus at sonic frequencies.

1. Introduction

Scaling from laboratory to seismic frequencies is not trivial, and there is imminent need for poroelastic properties at sonic frequencies (1 kHz). Although widely adapted, the so-called resonant bar techniques [e.g., *Demarest*, 1971; *Adams and Coppendale*, 1976] and forced oscillation methods [e.g., *Spencer*, 1981; *Batzle et al.*, 2006; *Subramaniyan et al.*, 2014] suffer from technical challenges and time-consuming sample preparation for measurements in the sonic and seismic range. Differential Acoustic Resonance Spectroscopy (DARS) is an attractive experimental method based on the change in resonance frequency of a fluid-filled tube by the introduction of a foreign object in the tube [*Harris*, 1996]. For a liquid with a sound velocity of 1 km/s, e.g., light oil, the resonance frequency of a 0.5 m open-ended submerged tube is 1 kHz. A benefit of the DARS data acquisition procedure is that the sample to be measured not needs to be machined to a specific geometry. The shape of the rock sample may even be irregular, as only its bulk volume is required.

The DARS method is based on the pressure perturbation of the empty tube due to the introduction of a foreign object in the tube. The density and compressibility of the foreign object differ from the values in the surrounding medium. The perturbation theory [*Morse and Ingard*, 1968] yields an expression for the perturbed normal mode due to the scattering of a small object within a resonator. The perturbed resonance frequency is determined by the root-mean-square (RMS) pressure distribution and the velocity distribution over the sample. This change in frequency is related to the change in compressibility of the system due to the introduction of a sample, which is related to the bulk modulus of this sample [*Harris*, 1996; *Xu*, 2007].

Previous work [*Chen et al.*, 2006; *Xu*, 2007; *Li and Wang*, 2010; *Wang et al.*, 2012; *Dong et al.*, 2013; *Zhao et al.*, 2013] on DARS concentrated on the improvement of the laboratory setup and data processing algorithms to extract (poro)elastic material properties from the original perturbation theory on purely elastic solids. Experimental evidence showed that the DARS setup provides a complimentary technique to measure the Gassmann undrained bulk modulus of jacketed and unjacketed porous samples at low frequencies [*Vogelaar et al.*, 2009; *Zhao et al.*, 2015]. *Wang et al.* [2012] implemented a finite element simulation to better understand the DARS system and to improve its accuracy in estimating the acoustic properties of elastic solids and a variety of polymers and rubber test samples with irregular shapes. *Zhao et al.* [2013] presented a whole-curve fitting inversion technique to estimate not only the compressibility but also the density of the samples.

Applications of the DARS method involve the estimation of seismic wave dispersion, acoustic attenuation, and fluid-flow properties in (partially) saturated reservoir rocks [*Harris et al.*, 2005; *Xu et al.*, 2006; *Chen et al.*, 2006; *Cong et al.*, 2008; *Zhao et al.*, 2014]. Recently, DARS is shown to be especially suitable for measuring the bulk modulus of irregular-shaped elastomers [*Wang et al.*, 2012]. Numerical simulations also yield the compressional and shear wave velocity in perfectly elastic media [*Li and Wang*, 2010; *Dong et al.*, 2013]. Inversion methods provide estimates of the compressibility and density of porous samples [*Zhao et al.*, 2013].

The principles of poroelasticity were generally applied to the experimental data in a heuristic approach [*Harris et al.*, 2005; *Xu et al.*, 2006; *Cong et al.*, 2008; *Vogelaar and Smeulders*, 2013]. The aim of current paper is to establish a theoretical justification for the laboratory measurements acquired with the DARS method. The usefulness of the theory is that the DARS method can provide complementary rock properties to the well-established techniques in the sonic range to bridge the gap between ultrasonic and seismic methods. In this letter, we show that bulk modulus of a variety of rock samples measured in DARS experiments are in quantitative agreement with the quasi-static theory of poroelasticity. We present the rigorous derivation of a quasi-static poroelastic model and compare the outcome with DARS measurements on porous, permeable rocks. This enables us to identify the relevant rock physical properties and to assess the merits and limitations of the DARS method.

2. Differential Acoustic Resonance Spectroscopy

2.1. Experimental Setup and Procedure

The resonator is an open-ended aluminum cylinder immersed in a fluid-filled tank. A layout of the equipment is shown in Figure 1. The cylinder has a length L of 0.38 m, an inner radius of 3.9 cm, and a wall thickness of 8 mm. The oil fills 0.64 m of the $0.23 \times 0.23 \times 0.70$ m tank (inner dimensions) having 13 mm thick Perspex walls. Pressure variations in the fluid are excited by piezoelectric sources. A hydrophone measures the pressure. The sources and receiving hydrophone are connected to a computer-controlled lock-in amplifier. A lock-in amplifier is a phase-sensitive detector that singles out the component of the received signal at a specific reference frequency and phase, using a predefined frequency sweep to select the resonance curve of the fundamental mode.

The length of the cylinder L and the sound velocity c_f of the fluid determine the resonance frequency. It is noted that the oil tank itself also has its own resonance frequency, depending among other factors on the fluid column. In our experiments, we use 5 cSt Dow Corning 200 silicone oil to fill the tank. A sound velocity of 975 m/s is measured using the spectral ratio method [*Toksöz et al.*, 1979]. Its density and viscosity are also measured independently to be 916 ± 1 kg/m^3 and 6.0 ± 0.2 mPa s.

The typical resonance frequency of the empty, fluid-filled, cylinder is measured to be 1083 Hz. It is easy to show that resonance will occur at $f_n = nc_f/2L$, for $n = 1, 2, 3, \ldots$. For our system, this would mean that the first harmonic $f_1 = 1280$ Hz. The difference is caused by the fact that the boundary condition of a pressure release surface at the open ends are not met exactly. Following *Pierce* [1989], the simplest end correction is to take the pressure release surface at $L + 2\Delta L$. From our experiments, we find that $\Delta L = 3.4$ cm. A more sophisticated correction would be to take the finite compliance of the cylinder and the quality factor of the system into account. The not perfectly rigid cylinder will cause the resonance frequency to drop from their theoretical value.

All tested objects are small cylindrical samples, having standard length $l = 3.7$ cm (1.5 inch) and standard diameter $d = 2.5$ cm (1 inch), except four samples that are slightly shorter. The measured object is hung on a thin nylon wire in the sources-receiver plane (the so-called pressure antinode) but can be moved vertically along the axis of the cylinder using the step motor. The computer-controlled step motor provides an accurate and repeatable positioning of the sample. The perturbed frequency is measured when a rock sample is located at the pressure antinode in the middle of the cylinder. Dependent on the sample properties, a typical perturbed resonance frequency is 1090 Hz.

2.2. Perturbation Theory

The perturbation theory derived here relates the shift in frequency (from empty resonance ω_f to sample-loaded resonance ω_e) to the sample properties. *Morse and Ingard* [1968] derived an expression for the perturbed normal mode due to the scattering of a small object of volume V_e within a resonator of volume V_f having sound velocity c_f. The foreign object has density ρ_e and effective bulk modulus K_e, different from the values in the surrounding fluid ρ_f and K_f, respectively.

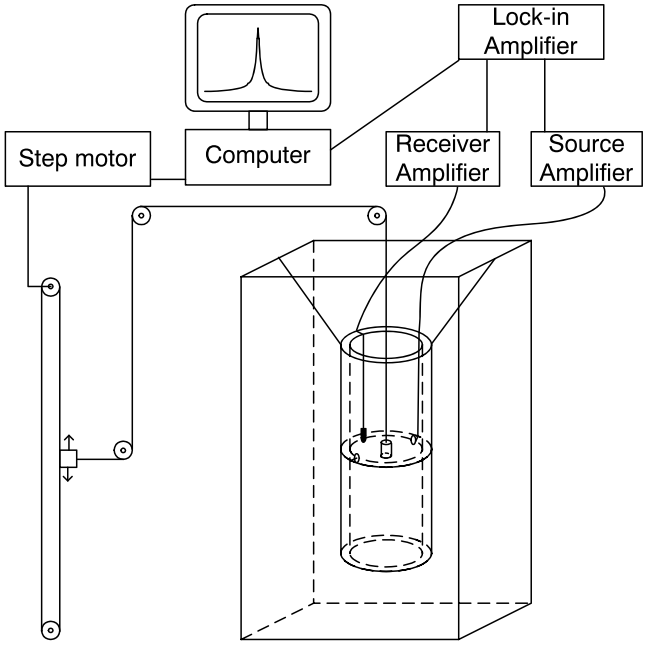

Figure 1. Layout of the DARS setup. The sources and receiving hydrophone are connected to a computer-controlled lock-in amplifier. The test object (small cylindrical sample) is hung on a thin nylon wire in the sources-receiver plane but can be axially moved using the computer-controlled step motor. This system was conceived and first built at the Stanford Wave Physics Laboratory [*Harris*, 1996].

The perturbed resonance frequency ω_e is determined by the RMS pressure-amplitude distribution p and the velocity-amplitude distribution v over the sample [*Morse and Ingard*, 1968; *Harris*, 1996; *Xu*, 2007]

$$\frac{\omega_e^2 - \omega_f^2}{\omega_f^2} \simeq -\frac{1}{\Lambda}\frac{V_e}{V_f}\left[\delta_K \langle p\rangle^2 + \delta_\rho \langle \rho_f^2 c_f^2 v^2\rangle\right], \tag{1}$$

where Λ is a calibration coefficient. The brackets around a quantity define the volumetric averaging operator and $V_e \ll V_f$. We define the difference in bulk modulus δ_K:

$$\delta_K = \frac{K_f - K_e}{K_e}, \tag{2}$$

and the difference in density δ_ρ

$$\delta_\rho = \frac{\rho_e - \rho_f}{\rho_e}. \tag{3}$$

If the object is heavier and stiffer than the displaced fluid, $\rho_e > \rho_f$ and $K_e > K_f$, the first term on the right-hand side in equation (1) tends to increase the resonance frequency and the second term tends to decrease the resonance frequency. When the measurements are performed at a velocity node ($v = 0$), the second term on the right-hand side of equation (1) may be neglected, and we write

$$\frac{\omega_e^2 - \omega_f^2}{\omega_f^2} \simeq -\frac{\langle p\rangle^2}{\Lambda}\frac{V_e}{V_f}\delta_K. \tag{4}$$

The complex-valued resonance frequency, $\omega_e = \omega_r + i\omega_i$, has a real component ω_r and an imaginary component ω_i. The imaginary resonance frequency is the half-width at half the maximum of the response function with which the resonance is monitored in a frequency domain experiment. Equation (4) means that a linear dependence between $(\omega_e^2 - \omega_f^2)/\omega_f^2$ and V_e may be expected, where the sample size rather than the sample shape is involved. Rewriting equation (2) using equation (4) gives the DARS bulk modulus of the sample

$$\frac{K_e}{K_f} = \left[1 - \frac{\omega_e^2 - \omega_f^2}{\omega_f^2}\frac{V_f}{V_e}\frac{\Lambda}{\langle p\rangle^2}\right]^{-1}. \tag{5}$$

Table 1. Rock Physical Properties of the Tested Samples[a]

Sample	k_0 (mD)	ϕ (–)	K_U (GPa)	K_{seal} (GPa)	K_{open} (GPa)	K_0 (GPa)	Q_{open} (–)
CHK03	$1.1 \cdot 10^0$	0.28	24.2 ± 1.2	26.0 ± 4.2	9.4 ± 0.6	3.0	74
CHK04	$1.1 \cdot 10^0$	0.28	24.0 ± 1.1		9.9 ± 0.7	3.0	85
SSA04	$3.6 \cdot 10^2$	0.21	9.6 ± 0.5	7.7 ± 0.4	3.9 ± 0.1	3.8	82
SSA11	$3.1 \cdot 10^2$	0.21	8.8 ± 0.4		4.1 ± 0.1	3.8	96
SSB04	$6.0 \cdot 10^3$	0.30	12.4 ± 0.6		2.7 ± 0.0	2.7	23
SSB07	$2.7 \cdot 10^3$	0.29	15.3 ± 0.7	11.9 ± 0.9	2.9 ± 0.0	2.9	38
SSB08	$4.0 \cdot 10^3$	0.30	12.3 ± 0.6		2.8 ± 0.0	2.8	27
SSB09	$2.7 \cdot 10^3$	0.28	15.7 ± 0.7		2.9 ± 0.0	2.9	36
SSC05	$7.4 \cdot 10^{-1}$	0.12	16.5 ± 0.8	14.0 ± 1.3	8.9 ± 0.5	6.3	59
SSC06	$9.5 \cdot 10^{-1}$	0.12	15.1 ± 0.7		5.8 ± 0.2	6.1	39
SSF02	$2.7 \cdot 10^3$	0.27	7.9 ± 0.4	6.3 ± 0.3	2.8 ± 0.0	3.1	31
SSF03	$2.5 \cdot 10^3$	0.27	8.7 ± 0.4		2.6 ± 0.0	3.1	27
SSF04	$2.1 \cdot 10^3$	0.27	7.7 ± 0.4		3.0 ± 0.0	3.1	27
SSG01	$1.9 \cdot 10^3$	0.24	9.5 ± 0.5	8.9 ± 0.5	3.2 ± 0.1	3.3	26
SSG02	$2.9 \cdot 10^2$	0.23	11.2 ± 0.5		3.3 ± 0.1	3.5	33
YBE03	$1.8 \cdot 10^2$	0.19	11.1 ± 0.5	9.5 ± 0.6	5.2 ± 0.2	4.2	112
VIF01	$1.2 \cdot 10^4$	0.38	5.2 ± 0.2	5.6 ± 0.2	2.2 ± 0.0	2.2	15
VIF02	$1.3 \cdot 10^4$	0.38	5.4 ± 0.3		2.2 ± 0.0	2.2	15
VIC05	$2.6 \cdot 10^4$	0.43	3.4 ± 0.2	3.5 ± 0.1	1.9 ± 0.0	2.0	14
VIC06	$2.8 \cdot 10^4$	0.42	3.5 ± 0.2		1.8 ± 0.0	2.0	8
QUE09	$2.2 \cdot 10^3$	0.22	10.1 ± 0.5	9.0 ± 0.5	3.2 ± 0.1	3.6	29
QUE10	$2.4 \cdot 10^3$	0.22	9.3 ± 0.4		4.1 ± 0.1	3.6	34
B1P13	$3.3 \cdot 10^2$	0.20	12.3 ± 0.4	8.7 ± 0.5	5.1 ± 0.2	4.0	118
B1P14	$3.2 \cdot 10^2$	0.20	10.9 ± 0.5		5.0 ± 0.2	3.9	123
CAS16	$5.5 \cdot 10^0$	0.19	8.8 ± 0.4	8.1 ± 0.4	8.2 ± 0.4	4.2	81
CAS17	$5.0 \cdot 10^0$	0.20	8.9 ± 0.4		6.7 ± 0.3	4.1	64
B1N20	$2.0 \cdot 10^2$	0.21	9.9 ± 0.5	7.3 ± 0.4	4.0 ± 0.1	3.9	95
B1N21	$2.1 \cdot 10^2$	0.20	10.1 ± 0.5		4.1 ± 0.1	4.0	90
COL23	$5.3 \cdot 10^{-1}$	0.12	14.8 ± 0.7	11.0 ± 0.8	8.0 ± 0.4	6.2	61
COL25	$7.7 \cdot 10^{-1}$	0.11	15.9 ± 0.8		8.5 ± 0.5	6.4	71
BEN27	$1.2 \cdot 10^3$	0.24	12.7 ± 0.6	11.4 ± 0.9	3.3 ± 0.1	3.3	53
BEN28	$1.1 \cdot 10^3$	0.24	12.7 ± 0.6		3.2 ± 0.1	3.3	49
B2P30	$1.6 \cdot 10^2$	0.20	12.8 ± 0.6	8.6 ± 0.5	5.1 ± 0.2	4.0	96
B2N32	$9.3 \cdot 10^1$	0.19	12.3 ± 0.6	9.9 ± 0.6	5.7 ± 0.2	4.1	116
B2N33	$1.1 \cdot 10^2$	0.19	12.1 ± 0.6		5.1 ± 0.2	4.1	96
FEL36	$1.0 \cdot 10^1$	0.23	12.1 ± 0.6	8.2 ± 0.4	5.9 ± 0.2	3.5	57
FEL37	$9.1 \cdot 10^0$	0.23	13.2 ± 0.6		5.6 ± 0.2	3.6	57
NIV44	$6.5 \cdot 10^3$	0.30	7.9 ± 0.4	10.4 ± 0.7	3.1 ± 0.1	2.7	24
NIV45	$8.1 \cdot 10^3$	0.32	7.1 ± 0.3		2.7 ± 0.0	2.6	22
UNK50	$9.0 \cdot 10^{-2}$	0.16	15.9 ± 0.8	11.8 ± 0.9	7.6 ± 0.4	4.9	62
UNK51	$2.0 \cdot 10^{-1}$	0.16	14.4 ± 0.7		7.9 ± 0.4	4.9	67
NN356	$1.5 \cdot 10^0$	0.17	13.9 ± 0.7	10.9 ± 0.8	8.2 ± 0.4	4.6	75
NN458	$5.8 \cdot 10^0$	0.16	20.0 ± 1.0	14.4 ± 1.4	11.4 ± 0.9	4.9	133
GL160	$1.8 \cdot 10^4$	0.34	8.8 ± 0.4	4.7 ± 0.1	2.4 ± 0.0	2.4	11
GL261	$1.8 \cdot 10^4$	0.36	10.0 ± 0.5	5.2 ± 0.2	2.4 ± 0.0	2.3	12

[a]Permeability k_0, porosity ϕ, and Gassmann undrained bulk modulus K_U are obtained from independent laboratory measurements. Moduli K_{open} and K_{seal} are measured using the DARS method with different surface conditions. K_0 is the static limit of K_{unjack}, cf. equation (A3). Q_{open} is the effective modulus ratio of the real part of K_{unjack} and twice the imaginary part of K_{unjack} at 1 kHz.

Using five solid reference samples, *Vogelaar* [2009] found that $\Lambda/\langle p \rangle^2 = 1.68 \pm 0.01$. The real part of the effective DARS bulk modulus $K_e(\omega_r)$ is calculated using the sample-loaded and empty resonance frequency. The imaginary part of the effective DARS bulk modulus $K_e(\omega_i)$ is calculated from the sample-loaded and empty half-width at half maximum response. $Q_e = K_e(\omega_r)/2K_e(\omega_i)$ is taken as the effective modulus ratio of the perturbed resonance frequency to the full-width at half the maximum response. Equation (5) shows that the sought effective bulk modulus of the sample is a fraction of the bulk modulus of the compressing fluid. This fraction is measured from the volume-normalized frequency perturbation for the sample.

2.3. Bulk Modulus Examples

We compare the bulk modulus of the sample obtained by the DARS technique with the undrained bulk modulus of the saturated rock. We define the Gassmann undrained bulk modulus [*Gassmann*, 1951]

$$K_U = H - \frac{4}{3}\mu, \tag{6}$$

in terms of the undrained compressional wave modulus $H = P + 2Q + R$ and the shear modulus μ. Explicit expressions of the poroelastic coefficients are given in terms of the bulk modulus of the pore fluid, K_f, the mineral modulus of the solid grains K_s, the drained bulk modulus K_D, and porosity ϕ, respectively, as [*Biot and Willis*, 1957]

$$\begin{aligned} P &= \frac{\phi K_D + (1-\phi)K'}{\phi'} + \frac{4}{3}\mu, \\ Q &= \frac{\phi K'}{\phi'}, \\ R &= \frac{\phi^2 K_f}{\phi'}, \end{aligned} \tag{7}$$

where $\phi' = \phi + K'/K_s$ and $K' = K_f(\alpha - \phi)$ are auxiliary parameters and $\alpha = 1 - K_D/K_s$ is the so-called Biot-Willis constant.

The rock physical properties of the investigated porous samples are measured with conventional methods. See *Vogelaar* [2009] for details. The measured porosity and steady state permeability are given in Table 1. The drained bulk modulus K_D and shear modulus μ are calculated from the porosity, dry rock density, and the dry compressional and shear wave velocities. The bulk modulus of the fluid is calculated from the measured fluid density ρ_f and velocity c_f. For the moduli of the solid grains, we simply assume the common mineral moduli of calcite (K_s = 70 GPa) for the chalk samples and quartz (K_s = 37 GPa) for all other samples. The Gassmann undrained bulk moduli, calculated from equation (6) using the said rock properties, are listed in Table 1. The error in K_U is solely attributed to the uncertainty in the measured dry velocities.

The DARS method is used to measure the DARS moduli of the tested samples using equation (5). All samples are vacuumed and fully saturated with 5 cSt silicone oil, which is identical to the fluid filling the container. For the purpose of this experiment, the pores of the tested samples are initially open (unjacketed), so that the pore fluid can communicate with the surrounding fluid. The second batch of measurements is on the same samples, but now with the outer surface carefully sealed (jacketed) by means of an epoxy resin. The measured open and sealed DARS moduli, K_{open} and K_{seal}, are also given in tabel 1. Their error reflects the uncertainty in coefficient Λ.

The Gassmann undrained bulk modulus versus the DARS bulk modulus of the open samples is shown in Figure 2a. We observe that this DARS bulk modulus is generally lower than the Gassmann undrained bulk modulus for all samples. The agreement is significantly improved in Figure 2b, where we crossplotted the DARS bulk modulus of the sealed samples and the Gassmann undrained bulk modulus.

In conclusion, the bulk modulus measured with DARS is dependent on whether or not the pore fluid is allowed to communicate with the surrounding fluid. The mechanism responsible for the bulk modulus measured with the DARS setup is a combination of the bulk modulus of the saturated frame and fluid flow. To further investigate this claim, we derive the frequency-dependent bulk modulus of a porous sphere with the boundary conditions relevant for our experimental configuration. We compare the theoretical outcome with the DARS bulk modulus of the open samples.

3. Quasi-Static Loading of a Porous Sphere

3.1. Physical Model

Consider first the response of a porous sphere fully saturated with a single fluid to a uniform external stress. The sample radius is taken as $a = \sqrt[3]{3V_e/4\pi}$. The aspect ratios of the measured samples are 1.5 to 1.1, and the sample being approximated as spherical is reasonable. If either $l/d \gg 1$ or $l/d \ll 1$, then we would be better off approximating the sample as an infinitely long cylinder or a slab, respectively.

When the porous sphere is subjected to the oscillating pressure field of the applied stress, the sphere will contract and expand. These oscillations generate waves on the mesoscopic scale, i.e., on the length scale

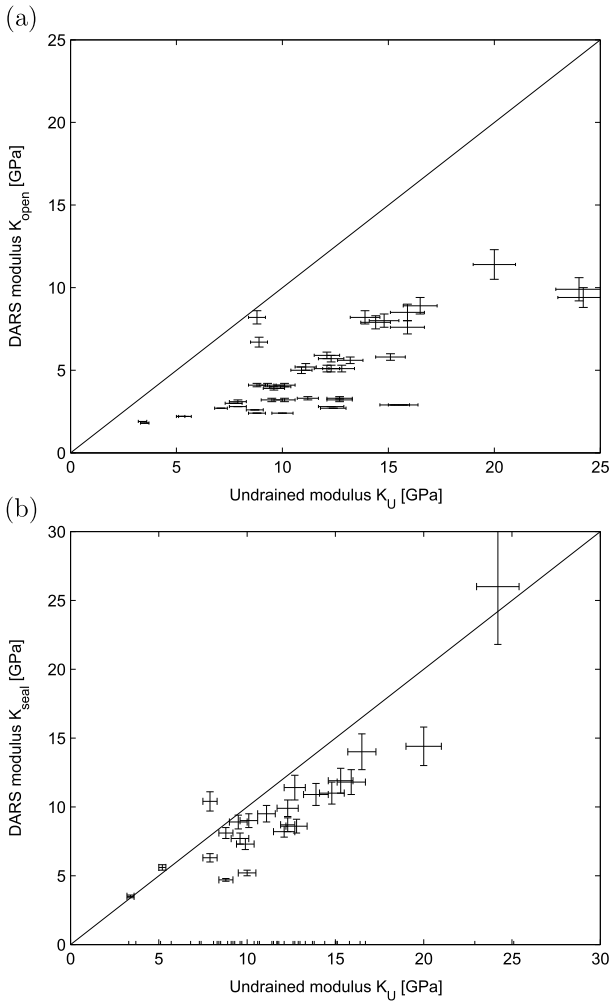

Figure 2. Crossplot of the Gassmann undrained bulk modulus K_U and the bulk modulus of the (a) open samples K_{open} and (b) sealed samples K_{seal} obtained by the DARS method.

of the sample [*Pride et al.*, 2004]. The external pressure field is assumed to be spatially homogeneous at the mesoscopic scale and the effective bulk modulus can be obtained by considering a representative volume comprising the porous medium and the surrounding liquid. The wave-induced pore pressure in the rock will be different from that in the surrounding liquid. The pressures will equilibrate via diffusive mechanisms. The characteristic frequency is determined by the diffusion time across the characteristic sample size a:

$$\omega_D \sim D/a^2, \tag{8}$$

where D is the slow wave diffusivity [*Johnson*, 2001]

$$D = \frac{k_0}{\eta\phi^2}\frac{PR - Q^2}{H}. \tag{9}$$

The rock properties are porosity ϕ and permeability k_0, and η is the fluid viscosity.

We presume that the frequency is low enough that the *Biot* [1956] theory is in its low-frequency limit (quasi-static case). Thus, the fast compressional wave is nondispersive and nonattenuating, whereas the slow compressional wave is diffusive in character. The requirement is $\omega \ll \omega_B$, where the Biot crossover frequency

$$\omega_B = \frac{\phi\eta}{k_0\alpha_\infty\rho_f}, \tag{10}$$

with tortuosity α_∞ and fluid density ρ_f.

The following derivation yields the relative fluid displacement as a function of the applied pressure and hence, the effective bulk modulus of the representative volume. The computation of the effective bulk modulus of the representative volume makes only sense if the frequency is low enough so that the wavelength of the external pressure wave is large compared to the dimensions of the introduced rock sample. That is, the mesoscopic condition $\omega \ll \omega_a$ should hold where

$$\omega_a \sim c_f/a. \tag{11}$$

The theory presented here thus assumes that $\omega_D \ll (\omega_B, \omega_a)$, so that one can investigate the crossover region from $\omega < \omega_D$ to $\omega > \omega_D$ without violating the low-frequency approximation [*Johnson*, 2001].

3.2. Governing Equations

The starting equations are essentially those of the Biot theory at low frequencies by simply setting to zero all higher-order inertial terms and by taking the dynamic permeability equal to its steady state value, k_0 [*Johnson*, 2001]. Adopting an $\exp(i\omega t)$ dependence for all relevant quantities, the quasi-static Biot equations are as follows:

$$\nabla \cdot \hat{\boldsymbol{\tau}} = 0, \tag{12}$$

$$\frac{k_0}{\eta\phi}\nabla\hat{p} = i\omega(\hat{\boldsymbol{u}} - \hat{\boldsymbol{U}}), \tag{13}$$

where **u** and **U** are the solid and fluid displacement, respectively. The total stress τ_{ij} (solid plus fluid phases) and pore fluid pressure p in terms of the solid and fluid strains, $e_{ij} = \nabla \cdot \hat{\boldsymbol{u}}$ and $\epsilon_{ij} = \nabla \cdot \hat{\boldsymbol{U}}$, are in the case of isotropic materials

$$\tau_{ij} = [(P + Q - 2\mu)e_{kk} + (Q + R)\epsilon_{kk}]\delta_{ij} + 2\mu e_{ij}, \tag{14}$$

$$-\phi p = Qe_{kk} + R\epsilon_{kk}. \tag{15}$$

3.3. General Solution

The spherically symmetric solutions to equations (12) and (13) obey the following equations [*Johnson*, 2001]:

$$\frac{\partial}{\partial r}\left[(P+Q)\left(\frac{\partial u}{\partial r} + \frac{2u}{r}\right) + (R+Q)\left(\frac{\partial U}{\partial r} + \frac{2U}{r}\right)\right] = 0, \tag{16}$$

and

$$\frac{i\omega\eta\phi^2}{k_0}(U-u) = \frac{\partial}{\partial r}\left[Q\left(\frac{\partial u}{\partial r} + \frac{2u}{r}\right) + R\left(\frac{\partial U}{\partial r} + \frac{2U}{r}\right)\right], \tag{17}$$

where u and U are the radial displacements of the solid and the fluid, respectively.

There are two different kinds of solutions to above equations: (1) Solutions for which the fluid motion is locked on to the solid's, $u(r)/U(r) = 1$, are linear combinations of r and r^{-2}. These are low-frequency fast compressional wave solutions. (2) Solutions for which $u(r)/U(r) = -(Q+R)/(P+Q)$ are linear combinations of spherical Bessel functions, $j_1(k_2r)$ and $n_1(k_2r)$, where k_2 $(= \sqrt{-i\omega/D})$ is the wave number of the slow-compressional Biot wave. At the quasi-static frequencies considered here, the slow wave is in fact a pure fluid pressure diffusion. For these solutions, the fluid and solid move out-of-phase, and the relevant quantities obey a diffusion equation with the slow-wave diffusivity given by equation (9). The general solution for the radial direction is written as follows [*Johnson*, 2001]:

$$u(r) = Ar + \frac{C}{r^2} + (Q+R)[Fj_1(k_2r) + Gn_1(k_2r)], \tag{18}$$

$$U(r) = Ar + \frac{C}{r^2} - (P+Q)[Fj_1(k_2r) + Gn_1(k_2r)], \tag{19}$$

$$p(r) = -\frac{3(Q+R)}{\phi}A + \frac{(PR-Q^2)}{\phi}k_2[Fj_0(k_2r) + Gn_0(k_2r)], \tag{20}$$

$$\tau(r) = 3K_U A - \frac{4\mu}{r^3}C - \frac{4\mu(Q+R)}{r}[Fj_1(k_2r) + Gn_1(k_2r)], \tag{21}$$

where A, C, F, and G are arbitrary constants to be determined from the appropriate boundary conditions.

3.4. Frequency-Dependent Bulk Modulus

The bulk modulus of a uniform solid, fluid, or porous material is generally denoted by the ratio of uniform compression $\hat{p}_e$ to the resulting relative volume change. As strain for a bulk solid, the relative volume change of a jacketed (sealed) porous sphere is given by its radius a and the radial solid displacement $\hat{u}(a)$ at the outer boundary ($r = a$), so that the bulk modulus is

$$K_{\text{jack}}(\omega) = -\frac{a}{3\hat{u}(a)}\hat{p}_e, \tag{22}$$

The movement of an interstitial fluid in a porous rock modifies its mechanical response to fluid loading. The relative volume change of the porous sample with open outer pores is dependent on its porosity. The bulk modulus of an unjacketed (open) porous sphere under fluid loading $\hat{p}_e$ is determined by the relative fluid-solid motion at the sample outer surface:

$$K_{\text{unjack}}(\omega) = -\frac{a}{3(\phi\hat{U}(a) + (1-\phi)\hat{u}(a))}\hat{p}_e, \tag{23}$$

where $\hat{U}(a)$ and $\hat{u}(a)$ are the radial fluid displacement and the radial solid displacement at the sample's surface having radius a. A closed-form analytical expression of K_{unjack} is found by using the solid and fluid displacement from equations (18) and (19). To guarantee a finite solution at $r = 0$, $C = G = 0$. There remain two arbitrary constants: A and F. The two boundary conditions at the open porous surface ($r = a$) are

$$\hat{p}(a) = \hat{p}_e, \tag{24}$$

$$\hat{\tau}(a) = -\hat{p}_e, \tag{25}$$

which yield

$$-\frac{3(Q+R)}{\phi}A + \frac{(PR-Q^2)}{\phi}k_2 F j_0(k_2 a) = \hat{p}_e, \tag{26}$$

$$3K_U A - \frac{4\mu(Q+R)}{a}F j_1(k_2 a) = -\hat{p}_e. \tag{27}$$

Adding both equations gives

$$A = \frac{4\mu(Q+R)j_1(k_2 a)/a - (PR-Q^2)k_2 j_0(k_2 a)/\phi}{3K_U - 3(Q+R)/\phi}F. \tag{28}$$

Subsequent substitution into equation (26) yields

$$F = \frac{Q+R-K_U\phi}{4\mu(Q+R)^2 j_1(k_2 a)/a - (PR-Q^2)K_U k_2 j_0(k_2 a)}\hat{p}_e. \tag{29}$$

Substitution of these constants into equations (18) and (19) gives for the frequency-dependent unjacketed bulk modulus of equation (23)

$$\frac{K_{\text{unjack}}(\omega)}{K_U} = \frac{3\left(\alpha^2/\gamma - \alpha B\right)j_1(k_2 a) - (1-\alpha B)\,k_2 a j_0(k_2 a)}{3\,(2\alpha - \gamma - \alpha B)\,j_1(k_2 a) - (1-\alpha B)\,k_2 a j_0(k_2 a)}, \tag{30}$$

in which Skempton's coefficient (undrained fluid pressure to confining-pressure ratio) is

$$B = \frac{Q+R}{\phi H}, \tag{31}$$

the Biot-Willis constant is

$$\alpha = \frac{\phi(Q+R)}{R}, \tag{32}$$

and

$$\gamma = \frac{\phi^2 K_U}{R}, \tag{33}$$

is an auxiliary coefficient. After some algebra, we find that in equation (30), the repeated term

$$1 - \alpha B = \frac{K_D}{K_U}. \tag{34}$$

As with other models with mesoscale mechanisms [*Pride et al.*, 2004], equation (30) means that the effective bulk modulus in the model is complex-valued and frequency dependent. An interesting aspect of a mesoscopic-scale model is that the slow wave number k_2 depends on the permeability of the medium modeled, as shown useful in the results.

4. Results

The real and imaginary values of the frequency-dependent unjacketed bulk modulus from equation (30) are shown in Figure 3 for six selected samples with a broad range in permeability. From the figure, we infer that at low frequencies, the real unjacketed bulk modulus of the sample approaches a lower bound. As shown in Appendix A, the effective static compressibility is the sum of the volume weighted compressibilities of the two constituents. The static limit K_0 is given in Table 1. At high frequencies, the real incompressibility of the sample goes to the Gassmann undrained bulk modulus K_U, as derived in Appendix B. Thus, the real and imaginary unjacketed bulk moduli show a typical relaxation process from the relaxed (drained) to the unrelaxed (undrained) response as the frequency increases. The static and no-flow moduli are also independent on the size of the sample as shown in the appendices.

All dependence on the size of the sample is thus restricted to the value of the characteristic diffusion frequency separating the low-frequency regime from the high-frequency regime. The crossover frequency from the low- to high-frequency regime is determined by the diffusion time across the sample. The characteristic diffusion frequency, equation (8), is linearly proportional to the permeability of the samples of equal effective size. The characteristic diffusion frequency ranges from < 0.1 Hz to > 1 kHz for present small samples with permeabilities from < 0.1 mD to > 10 Darcy.

Also, in Figure 3 is shown the experimental result from DARS measurements on the samples with open pores, K_{open}. For samples with a medium to high permeability ($k_0 > 10$ mD), we observe an excellent agreement between the (real) theoretical curves and experimental values. For the low-permeability samples (<10 mD), only a qualitative comparison can be made.

For the sake of completeness, the experimentally deduced values of Q_e for the open samples are shown also in Table 1. High-permeability, high-porosity samples show a low Q_{open} value, whereas medium to low-permeability and porosity samples generally have a high Q_{open} value. Effort on these apparent relationships is subject to future research.

5. Discussion

DARS experiments have been performed with the sample placed at the velocity node (pressure antinode), which is somewhere midway the open cylinder for the first harmonic mode [*Vogelaar*, 2009]. There are two points for the first harmonic within the cylinder where the compressibility and density contributions cancel and that the sample-loaded resonant frequency is identical to that of the empty cylinder. Extending the frequency range of the experiment to higher-order resonances is certainly possible, though the uniform acoustic pressure condition at the sample boundary becomes increasingly questionable for higher modes.

We note a clear difference between the DARS open pore measurements and the sealed pore measurements in Figure 2, which are attributed to the effects of the boundary condition on the amplitude of the Biot slow wave. That the acoustic properties of a system which includes a porous medium should depend on how the surface of that medium is prepared has been established on theoretical grounds quite some time ago [*Rosenbaum*, 1974]. The first experimental observation of the difference between open and sealed pores is by *Johnson et al.* [1994].

The examples in Figure 3 demonstrate that the value of the bulk modulus $K_{unjack}(\omega)$ in the model is principally controlled by the order of permeability of the sample. The larger the permeability, the greater the mesoscopic fluid pressure gradient and the greater the mesoscopic flow. The term mesoscopic is to be understood as larger than the typical pore size but smaller than the external wavelength.

For the high-permeability samples, the pore pressure is equilibrated with the external pressure at the measured DARS frequency. Pressure equilibration is quickly achieved by wave-induced fluid flow in the medium to high-permeability samples. When the characteristic diffusion frequency is on the same order of the external DARS frequency (1 kHz), the measured bulk modulus resides on the lower bound of the modeled

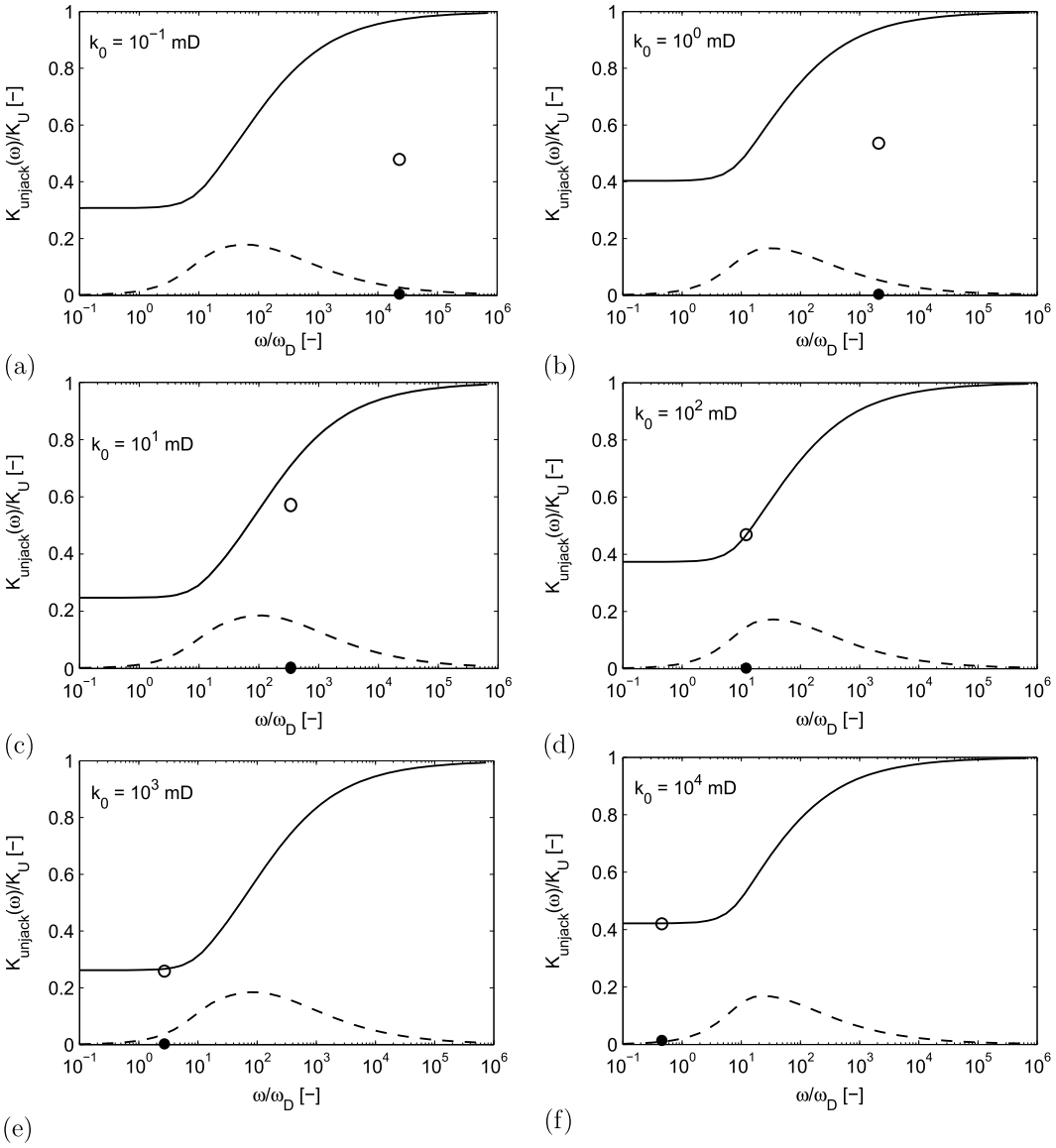

Figure 3. Comparison of the theoretical bulk modulus K_{unjack} (solid curve is the real part; dashed curve is the imaginary part) and experimentally measured DARS bulk modulus K_{open} (open circle is the real part; solid circle is the imaginary part) of open samples. (a) UNK50, (b) COL25, (c) NN458, (d) YBE03, (e) BEN27, and (f) VIF01. The selected samples are representative examples for their order of magnitude of the permeability k_0 as given. All bulk moduli are normalized by the Gassmann undrained bulk modulus K_U. The frequency is normalized by the characteristic diffusion frequency ω_D.

bulk modulus (Figures 3e and 3f). For medium-permeability samples (10–100 mD), the diffusion frequency is lower than the DARS frequency, so that the pore pressure equilibration via slow wave diffusion is limited.

For the low-permeability samples, the DARS frequencies is far above the characteristic diffusion frequency ($\omega/\omega_D > 10^2$), and the fluid pressure diffusion penetration distance becomes relatively small to the (mesoscopic) scale of the sample. As the frequency of the driving force is too high, the fluid has little time to flow and the results cannot adequately be described by slow wave diffusion. For these samples, the open pore boundary conditions are not fulfilled in practice. These samples act as if they were sealed and closed-pore boundary conditions apply, bringing the bulk modulus toward the jacketed bulk modulus of equation (22).

The one-data-point approach of *Wang et al.* [2012] also performs better with samples of high compressibility than those of low and medium compressibility. *Zhao et al.* [2013] expect that the DARS measurements with a sample at multiple locations inside the resonator will effectively suppress the errors caused by fluctuations

in experimental conditions or measurement uncertainty, thus contributing to more accurate estimates for samples of low compressibility.

If the interstitial fluid is prevented from escaping the pore network, the fluid loading of an open porous rock causes an increase in pore pressure, and this rise in pore pressure induces a dilatation of the rock. These coupled mechanisms bestow an apparent time-dependent character to the mechanical properties of the rock [*Detournay and Cheng*, 1993]. This diffusion-deformation mechanisms is earlier found in Figure 2, where the samples are less compliant under sealed conditions (when the pore fluid cannot escape the porous rock) than under open boundary conditions. Under open conditions, the excess pore pressure is completely dissipated in the high-permeability samples (relaxed condition), but not in the low-permeability samples where the pore fluid had not had time to flow between neighboring material elements (unrelaxed condition), other than within some local pore scale. If excess pore pressure induced by compression of the rock is allowed to dissipate through diffusive mass transport, further deformation of the rock progressively takes place.

Other dispersion mechanisms, such as a closed pore network and the presence of clay may play a role too in low-permeability stiff natural rocks. It is well known that the Biot theory accurately predicts velocities at seismic and cross-well frequencies (1 – 1000 Hz), but the global, macroscopic flow mechanism largely underestimates attenuation [*Mochizuki*, 1982]. This discrepancy is mainly due to mesoscopic inhomogeneities in the frame (e.g., interbedded shales) and in the fluid (e.g., gas patches) [*Pride et al.*, 2004]. The inhomogeneities can be grouped together and described by local pressure equilibration models. The external loading causes local pressure differences between the difference constituents. These differences are equilibrated by local, mesoscopic flow.

Finally, we note that treated section is a special solution in which we consider a sphere with open pores with uniform solid properties saturated by a single fluid. This paper also provides the general framework for other situations in which for example, the outer pores are sealed, the fluid consists of two phases such as gas and liquid (patchy theory), and porous materials in which the solid properties have a spatial distribution (double porosity dual permeability theory). These situations can be modeled by obeying relevant boundary conditions.

6. Conclusions

A theoretical analysis based on the quasi-static Biot theory confirms that the frequency-dependent unjacketed bulk modulus of high-permeability samples measured by DARS is controlled by the relative fluid-solid motion at the sample outer surface. The measured bulk modulus of these samples approaches a lower bound. This static limit is the sum of the volume weighted compressibilities of the two constituents. The measured bulk modulus of low-permeability samples increases toward the Gassmann undrained bulk modulus as is the case for jacketed porous samples (sealed pores at the outer surface). The high-frequency limit of the modeled quasi-static bulk modulus is equal to the Gassmann undrained bulk modulus because of the inherent no-flow condition at the sample surface. Hence, the DARS method at sonic frequencies (1 kHz) is particularly suitable to measure the bulk modulus of medium to high-permeability (>10 mD) samples where the pore pressure is equilibrated by slow-wave diffusion. The value of the bulk modulus in the model is principally controlled by the permeability of the sample via mesoscopic flow. Thus, in a practical but very elusive sense, the static and no-flow limit can be taken as two moduli to predict the sample porosity and permeability from DARS experiments in conjunction with the theory, or conversely, estimate the rock's effective bulk modulus and Q value, as done here.

Appendix A: Static Limit

The static limit of the unjacketed bulk modulus can be deduced directly from equation (30). For $\omega \to 0$, we have to use the asymptotic forms of the spherical Bessel functions with small arguments: $\lim_{z\to 0} j_0(z) = 1$, $\lim_{z\to 0} j_1(z) = z/3$ [*Abramowitz and Stegun*, 1965]. The static limit of $K_{\text{unjack}}(\omega)$ from equation (30) is

$$\lim_{\omega\to 0} \frac{K_{\text{unjack}}(\omega)}{K_{\text{U}}} = \frac{\left(\alpha^2/\gamma - 1\right)}{(2\alpha - \gamma - 1)}. \tag{A1}$$

A more accessible expression of K_0 is found by substituting K_{U}/γ with K_{f}/ϕ'. Using $\gamma = \phi' K_{\text{D}}/K_{\text{f}} + \alpha^2$ and $K_{\text{U}} = K_{\text{D}} + K_{\text{f}}\alpha^2/\phi'$ gives

$$\lim_{\omega\to 0} K_{\text{unjack}}(\omega) = \frac{K_{\text{D}}}{\phi' K_{\text{D}}/K_{\text{f}} + (\alpha - 1)^2}. \tag{A2}$$

With the definitions of ϕ' and α, this gives

$$\lim_{\omega\to 0} K_{\text{unjack}}(\omega) = K_0 = \left[\frac{\phi}{K_f} + \frac{1-\phi}{K_s}\right]^{-1}. \tag{A3}$$

In the static limit, the total stress is constant throughout the porous sample and equal to the applied external radial stress. The pore pressure is also everywhere the same and is equal to the pressure immediately outside the sample. Both solid and fluid components see the same stress, an isotropic external pressure. From equations (A11), (A15), and (A16), we confirm that

$$\lim_{\omega\to 0} \frac{p}{\hat{p}_e} = 1. \tag{A4}$$

Therefore, the effective compressibility of the sample is just the volume-weighted compressibilities of the two constituents, as in equation (A3). We realize that the bulk modulus is no longer a function of the sample radius a, thus independent of the spatial distribution of the sample volume V_e and fluid volume V_f.

The static limit of the bulk modulus can also be derived from the static limit of the *Biot* [1956] theory. The Biot equations of motion then reduce to [*Dutta and Odé*, 1979]

$$\frac{\partial}{\partial r}(\nabla\cdot\mathbf{u}) = 0, \tag{A5}$$

$$\frac{\partial}{\partial r}(\nabla\cdot\mathbf{w}) = 0. \tag{A6}$$

Note that we work here with relative displacement $w = \phi(\mathbf{U}-\mathbf{u})$. The solutions for spherically symmetric displacements are

$$u(r) = Ar + Cr^{-2}, \tag{A7}$$

$$w(r) = Fr + Gr^{-2}. \tag{A8}$$

Hence, we have for the pore pressure and total stress from equations (14) and (15) that

$$p = -\frac{Q+R}{\phi}\left(\frac{\partial u}{\partial r} + \frac{2u}{r}\right) - \frac{R}{\phi^2}\left(\frac{\partial w}{\partial r} + \frac{2w}{r}\right), \tag{A9}$$

$$\tau = H\frac{\partial u}{\partial r} + (H-2\mu)\frac{2u}{r} + \frac{Q+R}{\phi}\left(\frac{\partial w}{\partial r} + \frac{2w}{r}\right). \tag{A10}$$

A finite solution at $r = 0$ implies $C = 0$ and $G = 0$ and therefore,

$$p = -\frac{3(Q+R)}{\phi}A - \frac{3R}{\phi^2}F, \tag{A11}$$

$$\tau = 3K_U A + \frac{3(Q+R)}{\phi}F. \tag{A12}$$

We note that the pressure and total stress are no longer a function of r as a result of the displacement functions u and w specified in equations (A7) and (A8). Again, Q, R, and K_U are elastic constants of the rock. The remaining two unknowns A and F are determined by using the boundary conditions.

From the continuity of pressure and total stress at the boundary, equations (24) and (25), we have that

$$-\frac{3(Q+R)}{\phi}A - \frac{3R}{\phi^2}F = \hat{p}_e, \tag{A13}$$

and

$$3K_U A + \frac{3(Q+R)}{\phi} F = -\hat{p}_e. \tag{A14}$$

Adding both equations and using the coefficients from equations (32) and (33) gives

$$A = \frac{1-\alpha}{\gamma-\alpha} F. \tag{A15}$$

Subsequent substitution into equation (A13) yields

$$\frac{1-\alpha}{\gamma-\alpha}\frac{\alpha R}{\phi^2} + \frac{K_U}{\gamma} = -\frac{\hat{p}_e}{3F}. \tag{A16}$$

Substitution of these constants into equations (A7) and (A8) gives for equation (23)

$$\lim_{\omega\to 0} K_{\text{unjack}}(\omega) = \frac{-a}{3(u+w)}\hat{p}_e = \left[1 + \frac{1-\alpha}{\gamma-\alpha}\right]^{-1} \frac{-\hat{p}_e}{3F}. \tag{A17}$$

Inserting equation (A16) and normalization with K_U finally gives equation (A1).

The static limit of the jacketed bulk modulus from equation (22) is equal to the bulk modulus of the solid grains K_s (as in the unjacketed test, where the change in confining pressure produces an equal change in pore pressure) [*Vogelaar*, 2009].

Appendix B: No-Flow Limit

The high-frequency limit can also be deduced directly from equation (30). The asymptotic forms of the spherical Bessel functions with small arguments are $\lim_{z\to\infty} j_1(z)/j_0(z) = 0$ [*Abramowitz and Stegun*, 1965]. For $\omega \to \infty$, the frequency-dependent term $j_1(z)/j_0(z)$ vanishes, so that

$$\lim_{\omega\to\infty} K_{\text{unjack}}(\omega) = K_U, \tag{B1}$$

as expected (The modulus K_U is called the Gassmann undrained modulus because it is defined under the condition $\nabla \cdot \mathbf{w} = 0$, i.e., where fluid is not allowed to either enter or leave the sample during deformation).

We also consider the high-frequency limit of $K_{\text{unjack}}(\omega)$ under the assumption that the frequency is never so high as to violate $\omega \ll (\omega_B, \omega_a)$. As the frequency of the external stress becomes higher, the fluid has little time to flow. In case of the no-flow limit, the equations of motion become:

$$\frac{\partial}{\partial r}(\nabla \cdot \mathbf{u}) = 0, \tag{B2}$$

$$\mathbf{w} = 0, \tag{B3}$$

with the solution

$$u(r) = Ar + Cr^{-2}. \tag{B4}$$

Therefore, (cf. equations (A9) and (A10))

$$p = -\frac{3(Q+R)}{\phi} A, \tag{B5}$$

$$\tau(r) = 3K_U A - \frac{4\mu}{r^3} C. \tag{B6}$$

Again, $C = 0$ and the pore pressure and total stress are no longer a function of r. Continuity of total stress at the boundary (equation (25)) yields that

$$3K_U A = -\hat{p}_e. \tag{B7}$$

Substitution of the above in the solid displacement condition at the boundary yields that

$$u(a) = Aa = -\frac{\hat{p}_e}{3K_U} a, \tag{B8}$$

so that the effective bulk modulus in the high-frequency limit is given by equation (B1).

We realize that although the fluid pressure is constant within the rock and within the surrounding fluid, it is discontinuous at their boundary. Equations (B5)–(B7) then give

$$\lim_{\omega\to\infty}\frac{p}{\hat{p}_e}=\frac{Q+R}{\phi K_U}=\frac{HB}{K_U}=\frac{\alpha}{\gamma}. \tag{B9}$$

This fluid pressure discontinuity at the boundary is due to the different physical properties of the rock and fluid. The pore fluid pressure simply cannot catch up with the rapid external pressure variations. However, the total radial bulk stress is continuous, and since there is no relative fluid flow, the boundary acts as if it were jacketed. This case has also been discussed by *Vogelaar et al.* [2010] for patchy saturated media.

The no-flow limit of the jacketed bulk modulus from equation (22) is also equal to the Gassmann undrained bulk modulus K_U, as is expected from the so-called undrained test.

Acknowledgments

The work of B.V. was performed with financial support of ExxonMobil, Schlumberger, General Electric, and Toyota in the Global Climate and Energy Project (GCEP) when at Stanford University and with support of Shell Global Solutions International when at Eindhoven University of Technology. The rock physical data for the model are provided in section 2.3. The resonant frequency data are freely available through the Delft University of Technology Repository (http://repository.tudelft.nl/). We thank Jack Dvorkin for reviewing the original draft of the manuscript. B.V. is grateful to the two (slightly) anonymous reviewers for making several useful suggestions and critical corrections that improved the paper.

References

Abramowitz, M., and I. A. Stegun (1965), *Handbook of Mathematical Functions With Formulas, Graphs, and Mathematical Tables*, Dover, New York.

Adams, R. D., and J. Coppendale (1976), Measurement of the elastic moduli of structural adhesives by a resonant bar technique, *J. Mech. Eng. Sci.*, *18*(3), 149–158.

Batzle, M. L., D.-H. Han, and R. Hofmann (2006), Fluid mobility and frequency-dependent seismic velocity—Direct measurements, *Geophysics*, *71*, N1–N9, doi:10.1190/1.2159053.

Biot, M. A. (1956), Theory of propagation of elastic waves in a fluid-saturated porous solid: I. Low frequency range. II. High frequency range, *J. Acoust. Soc. Am.*, *28*, 168–191.

Biot, M. A., and D. G. Willis (1957), The elastic coefficients of the theory of consolidation, *J. Appl. Mech.*, *24*, 594–601.

Chen, D., X. Wang, J. Cong, D. Xu, Y. Song, and S. Ma (2006), Experimental studies on perturbed acoustic resonant spectroscopy by a small rock sample in a cylindrical cavity, *Sci. China Ser. G*, *49*(6), 683–701, doi:10.1007/s11433-006-0683-1.

Cong, J., X. Wang, D. Xu, D. Chen, and C. Che (2008), Experimental studies on the effects of porosity on acoustic resonance spectroscopy for synthetic porous rock samples in a cylindrical resonant cavity, *Chin. Sci. Bull.*, *53*, 978–983, doi:10.1007/s11434-008-0031-0.

Demarest, H. J. (1971), Cube-resonance method to determine the elastic constants of solids, *J. Acoust. Soc. Am.*, *49*, 768–775, doi:10.1121/1.1912415.

Detournay, E., and A. H.-D. Cheng (1993), Fundamentals of Poroelasticity, in *Comprehensive Rock Engineering: Principles, Practice and Projects*, vol. 2, edited by C. Fairhurst, pp. 113–171, Analysis and Design Method, Pergamon Press, New York.

Dong, C., S. Wang, J. Zhao, and G. Tang (2013), Numerical experiment and analysis of the Differential Acoustic Resonance Spectroscopy for elastic property measurements, *J. Geophys. Eng.*, *10*, 054002, doi:10.1088/1742-2132/10/5/054002.

Dutta, N. C., and H. Odé (1979), Attenuation and dispersion of compressional waves in fluid-filled porous rocks with partial gas saturation (White model): 1. Biot theory, *Geophysics*, *44*(11), 1777–1788.

Gassmann, F. (1951), Über die Elastizität poröser Medien, *Vierteljahrscr. Nat. Ges. Zür.*, *96*, 1–23.

Harris, J. M. (1996), Differential Acoustic Resonance Spectroscopy, Seismic Tomography Project Annual Report, Paper F, Stanford Univ., Stanford, Calif.

Harris, J. M., Y. Quan, and C. Xu (2005), Differential Acoustical Resonance Spectroscopy: An experimental method for estimating acoustic attenuation in porous media, *75th Annual Int. Meeting, SEG, Expanded Abstracts*, 1569–1572, Houston, Tex.

Johnson, D. L. (2001), Theory of frequency dependent acoustics in patchy-saturated porous media, *J. Acoust. Soc. Am.*, *110*, 682–694.

Johnson, D. L., T. J. Plona, and H. Kojima (1994), Probing porous media with first and second sound: II. Acoustic properties of water-saturated porous media, *J. Appl. Phys.*, *76*, 115–125.

Li, Y., and S. Wang (2010), Estimate the volume and compressibility of a small rock sample with Differential Acoustic Resonance Spectroscopy, *Int. Conference on Mechanical and Electronics Engineering*, *2*, 446–448, Kyoto, Japan.

Mochizuki, S. (1982), Attenuation in partially saturated rocks, *J. Geophys. Res.*, *87*, 8598–8604.

Morse, P. M., and K. U. Ingard (1968), *Theoretical Acoustics*, McGraw-Hill, New York.

Pierce, A. D. (1989), *Acoustics: An Introduction to Its Physical Principles and Applications*, Acoustical Society of America, Woodbury, New York.

Pride, S. R., J. G. Berryman, and J. M. Harris (2004), Seismic attenuation due to wave-induced flow, *J. Geophys. Res.*, *109*, B01201, doi:10.1029/2003JB002639.

Rosenbaum, J. H. (1974), Synthetic microseismograms: Logging in porous formations, *Geophysics*, *39*, 14–32.

Spencer, J. W. (1981), Stress relaxation at low frequencies in fluid saturated rocks: Attenuation and modulus dispersion, *J. Geophys. Res.*, *86*, 1803–1812, doi:10.1029/JB086iB03p01803.

Subramaniyan, S., B. Quintal, N. Tisato, E. H. Saenger, and C. Madonna (2014), An overview of laboratory apparatuses to measure seismic attenuation in reservoir rocks, *Geophys. Prospect.*, *62*(6), 1211–1223, doi:10.1111/1365-2478.12171.

Toksöz, M. N., D. H. Johnston, and A. Timur (1979), Attenuation of seismic waves in dry and saturated rocks. Part 1: Laboratory measurements, *Geophysics*, *44*(4), 681–690.

Vogelaar, B. B. S. A. (2009), Fluid effect on wave propagation in heterogeneous porous media, PhD thesis, Delft Univ. of Technology, Delft, Netherlands.

Vogelaar, B. B. S. A., and D. M. J. Smeulders (2013), Novel technique to measure the Biot-Gassmann modulus, *Poromechanics V: Proceedings of the Fifth Biot Conference on Poromechanics*, 173–182, Vienna, Austria, doi:10.1061/9780784412992.020.

Vogelaar, B. B. S. A., D. M. J. Smeulders, and J. M. Harris (2009), Experimental evidence of the relation between the Biot-Gassmann modulus and the bulk modulus measured by Differential Acoustic Resonance Spectroscopy of oil-saturated rocks, *79th Annual Int. Meeting, SEG, Expanded Abstracts*, 2189–2193, Houston, Tex.

Vogelaar, B. B. S. A., D. M. J. Smeulders, and J. M. Harris (2010), Exact expression for the effective acoustics of patchy saturated rocks, *Geophysics*, *75*, N87–N96.

Wang, S., J. Zhao, Z. Li, J. M. Harris, and Y. Quan (2012), Differential Acoustic Resonance Spectroscopy for the acoustic measurement of small and irregular samples in the low frequency range, *J. Geophys. Res.*, *117*, B06203, doi:10.1029/2011JB008808.

Xu, C. (2007), Estimation of effective compressibility and permeability of porous materials with Differential Acoustic Resonance Spectroscopy, PhD thesis, Stanford Univ., Stanford.

Xu, C., J. M. Harris, and Y. Quan (2006), Estimating flow properties of porous media with a model for dynamic diffusion, *76th Annual Int. Meeting, SEG, Expanded Abstracts*, 1831–1835, New Orleans, La.

Zhao, J., G. Tang, J. Deng, X. Tong, and S. Wang (2013), Determination of rock acoustic properties at low frequency: A Differential Acoustic Resonance Spectroscopy device and its estimation technique, *Geophys. Res. Lett.*, *40*, 2975–2982, doi:10.1002/GRL.50346.

Zhao, J., S. Wang, L. Li, W. Wei, and Y. Yin (2014), Studies on dispersion of reservoir rocks using multi-band direct laboratory measurement methodology with μ-CT scanning, *76th EAGE Conference and Exhibition*, 1–4, doi:10.3997/2214-4609.20141307, Amsterdam.

Zhao, J., S. Wang, H. Yin, X. Ma, X. Yan, and Z. Li (2015), Multi-band direct laboratory measurement-based dispersion analysis on reservoir rocks, *3rd Int. Workshop on Rock Physics*, 1–5, Perth, Australia.